

Excitation and Ionization Properties of Star-forming Galaxies at $z = 2.0 - 9.3$ with *JWST*/NIRSpec

RYAN L. SANDERS ^{1,*} ALICE E. SHAPLEY ² MICHAEL W. TOPPING,³ NAVEEN A. REDDY ⁴ AND
GABRIEL B. BRAMMER ^{5,6}

¹*Department of Physics and Astronomy, University of California, Davis, One Shields Ave, Davis, CA 95616, USA*

²*Department of Physics & Astronomy, University of California, Los Angeles, 430 Portola Plaza, Los Angeles, CA 90095, USA*

³*Steward Observatory, University of Arizona, 933 N Cherry Avenue, Tucson, AZ 85721, USA*

⁴*Department of Physics & Astronomy, University of California, Riverside, 900 University Avenue, Riverside, CA 92521, USA*

⁵*Cosmic Dawn Center (DAWN), Denmark*

⁶*Niels Bohr Institute, University of Copenhagen, Lyngbyvej 2, DK2100 Copenhagen Ø, Denmark*

ABSTRACT

We utilize medium-resolution *JWST*/NIRSpec observations of 164 galaxies at $z = 2.0 - 9.3$ from the Cosmic Evolution Early Release Science (CEERS) survey to investigate the evolution of the excitation and ionization properties of galaxies at high redshifts. Our results represent the first statistical constraints on the evolution of the [O III]/H β vs. [N II]/H α , [S II]/H α , and [O I]/H α “BPT” diagrams at $z > 2.7$, and the first analysis of the O₃₂ vs. R₂₃ diagram at $z > 4$ with a large sample. We divide the sample into five redshift bins containing 30 – 40 galaxies each. The subsamples at $z \sim 2.3$, $z \sim 3.3$, and $z \sim 4.5$ are representative of the main-sequence star-forming galaxy population at these redshifts, while the $z \sim 5.6$ and $z \sim 7.5$ samples are likely biased toward high specific star-formation rate due to selection effects. Using composite spectra, we find that each subsample at $z = 2.0 - 6.5$ falls on the same excitation sequence in the [N II] and [S II] BPT diagrams and the O₃₂-R₂₃ diagram on average, offset from the sequences followed by $z = 0$ H II regions in the same diagrams. The direction of these offsets are consistent with high-redshift star-forming galaxies uniformly having harder ionizing spectra than typical local galaxies at fixed nebular metallicity. The similarity of the average line ratios suggests that the ionization conditions of the interstellar medium do not strongly evolve between $z \sim 2$ and $z \sim 6$. Overall, the rest-optical line ratios suggest the $z = 2.7 - 9.3$ CEERS/NIRSpec galaxies at $\log(M_*/M_\odot) \sim 7.5 - 10$ have high degrees of ionization and moderately low oxygen abundances ($\sim 0.1 - 0.3 Z_\odot$), but are not extremely metal poor ($< 0.1 Z_\odot$) even at $z > 6.5$.

1. INTRODUCTION

Bright rest-frame optical emission lines are powerful tracers of the chemical and ionization state of the interstellar medium (ISM) of galaxies. The relative strengths of nebular emission lines of different metal ions and hydrogen recombination lines are determined by the physical properties of the ionizing source and ionized gas, including the shape of the ionizing spectrum, the ionization parameter (a combination of the intensity of the radiation field and the geometry of the gas relative to the ionizing source), and gas-phase metallicity.

In the local universe, many diagnostic line ratio diagrams have been established to probe the

physical conditions of the ionized ISM. Diagrams plotting [O III] λ 5008/H β vs. [N II] λ 6585/H α , [S II] λ 6718,6733/H α , and [O I] λ 6302/H α have been used to differentiate normal H II regions and star-forming galaxies ionized by massive stars from sources with other ionization mechanisms, including active galactic nuclei (AGNs) (Baldwin et al. 1981; Veilleux & Osterbrock 1987; Kauffmann et al. 2003; Kewley et al. 2006). We refer to these line-ratio diagrams as the [N II], [S II], and [O I] “BPT” diagrams, respectively. Within the [N II] BPT diagram, $z \sim 0$ star-forming galaxies follow a narrow sequence from high-[O III]/H β and low-[N II]/H α to low-[O III]/H β and high [N II]/H α . This sequence represents a progression of increasing metallicity and decreasing levels of excitation and ionization, and also constitutes a sequence of increasing stellar mass (M_*) reflecting the mass-metallicity relation (Tremonti et al. 2004; Curti et al. 2020). Local star-forming galax-

email: rlsand@ucdavis.edu

* NHFP Hubble Fellow

ies and H II regions follow similar well-defined sequences in the [S II] and [O I] BPT diagrams.

The location of the star-forming galaxy sequence in the [N II] BPT diagram evolves with redshift toward higher [N II]/H α at fixed [O III]/H β , or equivalently higher [O III]/H β at fixed [N II]/H α , between $z \sim 0$ and $z \sim 2.3$ (Steidel et al. 2014; Shapley et al. 2015, 2019; Sanders et al. 2016; Strom et al. 2017, 2018; Kashino et al. 2017, 2019). This offset from the local sequence appears to steadily increase with redshift over this redshift range (Shapley et al. 2019). The distinct line ratio excitation sequences followed by high- and low-redshift galaxies implies that at least some of the physical conditions within H II regions that regulate nebular line production evolve with redshift. Recent work has converged on the evolution of the ionizing spectral shape at fixed nebular metallicity as the primary driver of the $z \sim 2$ [N II] BPT diagram offset, with any change in ionization parameter, electron density, and/or N/O abundance ratio playing only minor roles (Steidel et al. 2016; Strom et al. 2018; Shapley et al. 2019; Topping et al. 2020a,b; Sanders et al. 2020; Runco et al. 2021). The different set of ionization properties at low and high redshifts has important implications for diagnostic calibrations used to translate line ratios to physical properties such as gas-phase metallicity that are of key importance for understanding galaxy evolution. Because the ionization conditions differ at $z \sim 0$ and $z \sim 2$, deriving accurate metallicities for high-redshift samples requires a different set of metallicity calibrations from those based on typical $z \sim 0$ H II regions and star-forming galaxies (e.g., Sanders et al. 2020).

Another important diagnostic diagram relates the O_{32} ($[\text{O III}]\lambda 5008/[\text{O II}]\lambda 3728$) and R_{23} ($([\text{O III}]\lambda\lambda 4960, 5008 + [\text{O II}]\lambda 3728)/\text{H}\beta$) line ratios. O_{32} serves as a relatively direct proxy of the degree of ionization while R_{23} is primarily sensitive to gas-phase metallicity. The O_{32} - R_{23} diagram has been studied out to $z \sim 3.3$, with high-redshift galaxies generally displaying higher O_{32} and R_{23} values on average relative to local galaxies (e.g., Nakajima & Ouchi 2014; Sanders et al. 2016; Strom et al. 2017; Onodera et al. 2016), associated with their lower metallicities due to the evolving mass-metallicity relation (Sanders et al. 2021). In this diagram, a harder ionizing spectrum pushes the maximum R_{23} ratio to higher values and generally increases R_{23} at fixed O_{32} (Steidel et al. 2016). Star-forming galaxies also follow a metallicity sequence in the O_{32} - R_{23} diagram from low- R_{23} and low- O_{32} at high metallicity to high- R_{23} and high- O_{32} at low metallicity, though R_{23} turns over and begins decreasing at very low metallicity ($\lesssim 0.1 Z_{\odot}$; e.g., Kewley et al. 2019).

These line ratios are commonly used as tracers of ISM chemical abundance (e.g., Maiolino et al. 2008; Troncoso et al. 2014; Onodera et al. 2016; Sanders et al. 2021).

Before the advent of *JWST*, ground-based observations of rest-optical emission lines at high redshift were limited to $z < 2.7$ for the BPT diagrams, and $z < 3.8$ for the O_{32} - R_{23} diagram, where the necessary lines fall bluewards of the red edge of the near-infrared K -band at $2.4 \mu\text{m}$. Spectroscopic instruments onboard *JWST* now provide the ability to measure rest-optical lines at much higher redshifts, with the NIRSpec instrument covering H α , [N II] and [S II] out to $z = 6.5$, and [O III] and H β out to $z = 9.3$. Recent studies of *JWST* spectra have provided the first glimpses into the metallicity and ionization properties of the ISM at $z = 4 - 8$ based on rest-optical emission lines (e.g., Curti et al. 2023; Brinchmann 2022; Schaerer et al. 2022; Arellano-Córdova et al. 2022; Taylor et al. 2022; Wang et al. 2022; Trump et al. 2022; Tacchella et al. 2022), but these studies are based on small numbers of targets and their relation to the typical galaxy population is unclear.

In this paper, we use *JWST*/NIRSpec spectroscopy of a sample of 164 galaxies at $z = 2.0 - 9.3$ to study the excitation and ionization properties of star-forming galaxies over cosmic time in diagnostic line ratio diagrams. This is the first such study to employ a large statistical sample of galaxies, with particularly novel investigations of the BPT diagrams at $z > 2.7$ and the O_{32} - R_{23} diagram at $z > 4$. This paper is organized as follows. In Section 2, we describe the observations, data reduction, measurements, and derived quantities. We characterize the properties of the sample and the position of star-forming galaxies in diagnostic line-ratio diagrams in Section 3, investigating the BPT diagrams in Sec. 3.2 and the O_{32} - R_{23} diagram in Sec. 3.3. We discuss the implications of our findings in Section 4.

Throughout this paper, we adopt a Chabrier (2003) initial mass function (IMF), Asplund et al. (2021) solar abundance, and a cosmology described by $H_0 = 70 \text{ km s}^{-1} \text{ Mpc}^{-1}$, $\Omega_m = 0.30$, and $\Omega_{\Lambda} = 0.7$. We provide vacuum rest-frame emission-line wavelengths. The line ratios analyzed in this work are defined as follows:

$$[\text{O III}]/\text{H}\beta = [\text{O III}]\lambda 5008/\text{H}\beta \quad (1)$$

$$[\text{N II}]/\text{H}\alpha = [\text{N II}]\lambda 6585/\text{H}\alpha \quad (2)$$

$$[\text{S II}]/\text{H}\alpha = [\text{S II}]\lambda\lambda 6718, 6733/\text{H}\alpha \quad (3)$$

$$[\text{O I}]/\text{H}\alpha = [\text{O I}]\lambda 6302/\text{H}\alpha \quad (4)$$

$$O_{32} = [\text{O III}]\lambda 5008/[\text{O II}]\lambda 3728 \quad (5)$$

$$R_{23} = \frac{[\text{O III}]\lambda\lambda 4960, 5008 + [\text{O II}]\lambda 3728}{\text{H}\beta} \quad (6)$$

2. OBSERVATIONS AND MEASUREMENTS

We use public data from *JWST*/NIRSpec Micro-Shutter Array (MSA) observations obtained as a part of the Cosmic Evolution Early Release Science (CEERS) survey (Program ID: 1345 Finkelstein et al. 2022a,b). Medium-resolution spectroscopy was obtained using the G140M/F100LP, G235M/F170LP, and G395/F290LP grating and filter combinations for six pointings in the AEGIS field, providing a spectral resolution of $R \sim 1000$ spanning wavelengths of $1 - 5 \mu\text{m}$. Each grating configuration was observed for 3107 sec of on-source integration per pointing, divided into three exposures of 14 groups, with the NRSIRS2 readout mode. Three MSA shutters were opened on each target to form slitlets of approximately $1.5'' \times 0.2''$, and a 3-point nod pattern was adopted. Each multi-object slitmask contained between 52 and 55 primary targets. In total, 318 unique sources were targeted, with three galaxies observed twice on two different masks.

2.1. Data Reduction

The data in all grating configurations were reduced using the following method. The individual uncalibrated detector images were first passed through *JWST* `calwebb_detector` pipeline¹, in which bias and dark current were removed and saturated pixels and cosmic ray artifacts (e.g., “showers” and “snowballs”) were masked. The resulting images were then corrected for striping by subtracting an estimate of the $1/f$ noise in each image. The 2D spectrum for each slitlet was then cut out. A flat-field correction, background subtraction based on dithered exposures, photometric calibration, and wavelength solution were applied using the latest calibration reference data system (CRDS) context (`jwst_1027.pmap`). The cutout 2D spectrum for each target was rectified and interpolated onto a wavelength grid that was common for all observations in a particular grating configuration. The calibrated 2D cutouts for each exposure were then combined based on the three-point dither pattern excluding pixels that were masked. Error spectra were derived by combining the variances from Poisson noise, read noise, and flat-fielding, and the variance between each individual exposure. This process yielded viable 2D science and error spectra for 310 targets in each grating and detector combination. For each grating configuration, the fully calibrated and rectified 2D spectra from both detectors were combined into a single 2D spectrum spanning the full wavelength range including the chip gap.

One-dimensional science and error spectra were extracted from the rectified 2D spectra using an optimal extraction (Horne 1986). The spatial profile was obtained by manually identifying wavelength ranges in the 2D spectrum containing high-S/N emission lines when present or detected continuum otherwise and summing the corresponding columns of the 2D spectrum. A Gaussian profile was then fit to the resulting spatial profile, and the best-fit Gaussian model was used to calculate the weights in the optimal extraction scheme. The extraction was limited to the range of cross-dispersion pixels around the peak where the spatial profile was positive. The extraction windows were typically 5 pixels or $0.5''$ in extent along the slit, approximately the size of one microshutter. During the extraction, wavelength ranges in which the extracted 1D spectrum was affected by unremoved cosmic rays, artifacts, or emission from neighboring serendipitously detected sources were manually identified and masked. The chip gap was also automatically identified and masked. All masked wavelength ranges were considered to have no coverage during the subsequent emission-line fitting. For many targets, spatial profiles could only be obtained for one or two grating configurations in which lines or continuum was detected, while the other gratings showed no significant detections from which to construct the profile. In such cases, the mean centroid, FWHM, and extraction window of the manually extracted grating(s) were used to automatically extract spectra from the gratings that lacked detections. 1D spectra were not extracted for targets for which there were no visible detections in any grating configuration. Out of 310 total targets, 1D spectra were extracted for 252 sources.

A wavelength-dependent slit-loss correction was then applied to the 1D spectra, described in detail in Reddy et al. (2023, in prep.). The intrinsic morphology of each target was estimated from *JWST*/NIRCam F115W imaging when available, or from a Sérsic profile fit to HST/WFC3 F160W imaging otherwise (van der Wel et al. 2014). If a target lacked robust shape constraints from *JWST* and HST imaging, then it was assumed to be a point source. At each wavelength, the fraction of total light falling inside an area defined by the width of the slit and the vertical extraction window was then estimated using the position of the target in the slitlet and the intrinsic morphology convolved with the wavelength-dependent *JWST*/NIRSpec point spread function. The 1D spectrum was then divided by this fraction as a function of wavelength.

The final flux calibration was achieved by scaling the 1D science spectra to match the photometric SEDs in the following way. The slit-loss corrected 1D spectra

¹ <https://jwst-pipeline.readthedocs.io/en/latest/index.html>

were passed through the filter transmission curves for the set of photometric bandpasses available for each target to produce synthetic photometric flux densities and errors. The ratio of the image-based and synthetic flux densities was calculated for each filter in which both the synthetic and image-based photometric measurements had $S/N > 5$. If the number of filters meeting this requirement was greater than or equal to 3, then the 1D spectra and error spectra in all grating configurations were scaled by the median of the individual ratios to achieve the final flux calibration. For the 109 targets that did not meet this criterion, no scale factor was applied. For the remaining 143 targets, the median scale factor was 0.997 with a standard deviation of 0.23 dex, implying that the absolute flux calibration is robust and that flux calibration of targets for which a scale factor was not applied should not be biased on average.

2.2. Emission Line Measurements

Emission line fluxes were measured from the 1D science spectra using the following method. For each target, the redshift was first measured using the best-fit centroid from a single Gaussian fit to the line with the highest signal-to-noise ratio, usually [O III] λ 5008 (57%) or H α (36%). The intrinsic velocity FWHM of the highest signal-to-noise line (corrected for instrumental resolution) was also calculated from the best-fit Gaussian profile. The instrumental resolution as a function of wavelength in each NIRSpec grating configuration was obtained from the dispersion curves distributed in the *JWST* User Documentation.² For the extracted 1D science spectrum in each grating configuration, lines that fell within the covered wavelength range were then fit with Gaussian profiles for which the centroid was restricted to be within 50 km s⁻¹ of the expected observed wavelength based on the measured redshift, while the FWHM was restricted to be within 20% of the expected FWHM in Å calculated by convolving the intrinsic velocity FWHM measured above with the instrumental resolution at the expected line centroid and converting from km s⁻¹ to Å. Adjacent lines separated by $\Delta\lambda$ at wavelength λ with $\Delta\lambda/\lambda < 0.01$ (e.g., [N II] λ 6550, H α , and [N II] λ 6585) were fit simultaneously with multiple Gaussians, while more widely separated lines were fit individually. Closely spaced lines that are blended and unresolvable at $R \sim 1,000$ (e.g., [O II] λ 3727,3730; [Ne III] λ 3970 and H ϵ ; He I λ 3890 and H ζ) were fit with a single Gaussian for which the FWHM restriction is relaxed to 50%. The continuum model was taken to

be the best-fit SED model (see Sec. 2.3 below), where the only free parameter is an additive offset. Using the best-fit SED model as the continuum has the advantage of self-consistently accounting for stellar Balmer absorption such that the measured H recombination line fluxes are robust.

Neighboring NIRSpec medium-resolution gratings have overlapping wavelength coverage such that the same emission line was measured in two gratings for 90 unique targets. Line fluxes measured in two gratings showed good agreement, with a median offset of 0.02 dex and an intrinsic scatter of 0.08 dex, suggesting that the relative flux calibration between grating configurations is robust on average. The final measured line flux was taken to be the inverse-variance weighted mean of the fluxes measured in each grating when a line was covered in two configurations.

2.3. Photometry and SED Fitting

Stellar population parameters including stellar mass are inferred by modeling the spectral energy distribution of each target using extensive multi-wavelength photometric catalogs. For 99 targets that were covered by CEERS *JWST*/NIRCam imaging taken in June 2022 (Finkelstein et al. 2022b), we used the catalog assembled by G. Brammer³. This catalog includes aperture-matched measurements in 7 *JWST*/NIRCam filters (F115W, F150W, F200W, F277W, F356W, F410M, and F444W) and 7 HST/ACS and WFC3 filters (F435W, F606W, F814W, F105W, F125W, F140W, and F160W), spanning $\sim 0.4 - 5 \mu\text{m}$ in the observed frame. A further 185 targets have measurements in the 3D-HST photometric catalogs (Momcheva et al. 2016; Skelton et al. 2014) spanning observed-frame $0.4 - 8 \mu\text{m}$ that we used for SED fitting. The remaining 35 CEERS medium-resolution NIRSpec targets had no coverage in the Brammer catalog and no reliable counterpart in the 3D-HST catalog, such that stellar population properties could not be derived for these targets. Of the 231 galaxies with robust NIRSpec spectroscopic redshifts, robust photometric SED information was available for a total of 210.

The SED fitting code FAST (Kriek et al. 2009) was used to fit the flexible stellar population synthesis models (FSPS; Conroy et al. 2009) to the measured photometry. We assumed a Chabrier (2003) IMF, delayed- τ star-formation histories of the form $\text{SFR} \propto t \times e^{-t/\tau}$, and two possible combinations of stellar metallicity and dust attenuation curve to reflect the chemical matu-

² <https://jwst-docs.stsci.edu/jwst-near-infrared-spectrograph/nirspec-instrumentation/nirspec-dispersers-and-filters>

³ <https://s3.amazonaws.com/grizli-v2/JwstMosaics/v4/index.html>

rity of galaxies in different redshift and stellar mass regimes, following Reddy et al. (2018) and Du et al. (2018). As described in Shapley et al. (2023), we assumed $Z_* = 0.02$ ($1.4 Z_\odot$) and the Calzetti et al. (2000) attenuation curve for all galaxies at $z \leq 1.4$ and for galaxies at $1.4 < z \leq 2.7$ ($2.7 < z \leq 3.4$) with masses above $10^{10.45} M_\odot$ ($10^{10.66} M_\odot$). For galaxies below these respective cutoff masses at $1.4 < z \leq 2.7$ and $2.7 < z \leq 3.4$, and for all galaxies at $z > 3.4$, we assumed $Z_* = 0.0031$ ($0.27 Z_\odot$) and the SMC extinction curve of Gordon et al. (2003). Before fitting, the contribution of nebular emission lines to the photometric flux densities was removed based on line fluxes measured from the NIRSpectra spectra, using the method described in Sanders et al. (2021). The output of the SED fitting includes inferred values and uncertainties for stellar mass, star-formation rate (SFR(SED)), continuum reddening, and stellar population age.

2.4. Reddening Correction, SFR, and Line Ratios

The amount of dust reddening ($E(B - V)_{\text{gas}}$) was inferred from the Balmer decrement $\text{H}\alpha/\text{H}\beta$ (Shapley et al. 2023) using the Milky Way extinction curve (Cardelli et al. 1989), which is consistent with direct constraints on the nebular attenuation curve at $z \sim 2$ (Reddy et al. 2020). We assumed an intrinsic ratio of $\text{H}\alpha/\text{H}\beta = 2.79$, calculated with `pyneb` (Luridiana et al. 2015) for an electron temperature of $T_e = 15,000$ K that is typical of high-redshift moderately low-metallicity sources (e.g., Sanders et al. 2020; Curti et al. 2023). For targets at $z > 6.5$ for which $\text{H}\alpha$ was not covered, $E(B - V)_{\text{gas}}$ was derived from $\text{H}\gamma/\text{H}\beta$ assuming an intrinsic ratio of 0.47. SFR($\text{H}\alpha$) was derived from the dust-corrected $\text{H}\alpha$ luminosity using a metallicity-dependent conversion factor based on BPASS population synthesis models including binary effects, where galaxies in the $1.4 Z_\odot + \text{Calzetti}$ case above use a $Z_* = 0.02$ conversion factor of $10^{-41.37} (M_\odot \text{yr}^{-1}) / (\text{erg s}^{-1})$, while those in the $0.27 Z_\odot + \text{SMC}$ case use a $Z_* = 0.001$ conversion factor of $10^{-41.67} (M_\odot \text{yr}^{-1}) / (\text{erg s}^{-1})$. For $z > 6.5$ galaxies, we instead infer SFR($\text{H}\beta$) from the dust-corrected $\text{H}\beta$ luminosity using the low-metallicity conversion factor assuming $\text{H}\alpha/\text{H}\beta = 2.79$.

Emission-line ratios were calculated from the measured line fluxes. Ratios of closely-spaced lines (e.g., $[\text{N II}]/\text{H}\alpha$, $[\text{O III}]/\text{H}\beta$, $[\text{S II}]/\text{H}\alpha$, $[\text{O I}]/\alpha$) were not corrected for dust reddening and measurement of these ratios thus has no requirement of a robust $E(B - V)_{\text{gas}}$ constraint. For ratios involving lines significantly separated in wavelength (e.g., O_{32} , R_{23}), line fluxes were first corrected for dust attenuation using the $E(B - V)_{\text{gas}}$ values derived above and assuming the Cardelli et al.

(1989) curve. As such, O_{32} and R_{23} were only measured for sources with $\text{S/N} \geq 3$ detections of either $\text{H}\alpha$ and $\text{H}\beta$, or $\text{H}\beta$ and $\text{H}\gamma$, for robust $E(B - V)_{\text{gas}}$ constraints. Uncertainties on reddening, SFR, and line ratios were estimated from the interior 68th-percentile of distributions derived by perturbing the observed line fluxes by their uncertainties, rederiving $E(B - V)_{\text{gas}}$, and recalculating SFR and all line ratios 5000 times.

2.5. Sample selection

For this analysis, we began by selecting the 172 galaxies with robust spectroscopic redshifts at $z \geq 2.0$. Eight targets were removed from the sample as candidate AGN based on the presence of broad emission around bright lines or measured $[\text{N II}]/\text{H}\alpha > 0.5$. We divided the resulting sample of 164 galaxies into 5 bins in redshift containing roughly equal number of sources, and refer to these bins based on the median redshift of sources in each. The sample analyzed in this work has 29 galaxies at $2.0 \leq z < 2.7$ ($z \sim 2.3$); 29 galaxies at $2.7 \leq z < 4.0$ ($z \sim 3.3$); 36 galaxies at $4.0 \leq z < 5.0$ ($z \sim 4.5$); 43 galaxies at $5.0 \leq z < 6.5$ ($z \sim 5.6$); and 27 galaxies at $6.5 \leq z < 9.3$ ($z \sim 7.5$). The full suite of rest-optical lines ($[\text{O II}]$ to $[\text{S II}]$) is covered for the lower four redshift bins, while the $z > 6.5$ bin lacks coverage of the redder rest-optical lines ($[\text{O I}]$, $\text{H}\alpha$, $[\text{N II}]$, and $[\text{S II}]$). In each line ratio vs. line ratio diagram, we plot galaxies with $\text{S/N} \geq 3$ for the relevant lines for both ratios as detections, while sources with a non-detection that provides a one-sided limit in one ratio while the lines of the other ratio are detected are plotted as 3σ limits.

2.6. Composite Spectra

Weak lines such as $[\text{N II}]$, $[\text{S II}]$, and $[\text{O I}]$ are not detected in many of the individual spectra. We construct composite spectra in different redshift bins using the following method to assess sample-averaged line ratios including information from galaxies for which all necessary lines are not detected. For each object in a bin, the 1D spectra from each grating configuration are first normalized by the measured $\text{H}\alpha$ flux and shifted to the rest frame. The spectra are then linearly interpolated onto a uniform wavelength grid with spacing equal to the minimum rest-frame wavelength sampling of all targets in the bin determined by the G140M sampling of the highest-redshift source in the bin. The 1D spectra in each grating configuration are then combined into a single 1D spectrum, where the inverse-variance weighted mean is used to combine values at wavelengths where there is overlap between two neighboring gratings. Once these steps have been completed for all targets, the composite spectrum is computed by taking the median value of the individual combined 1D spectra at each

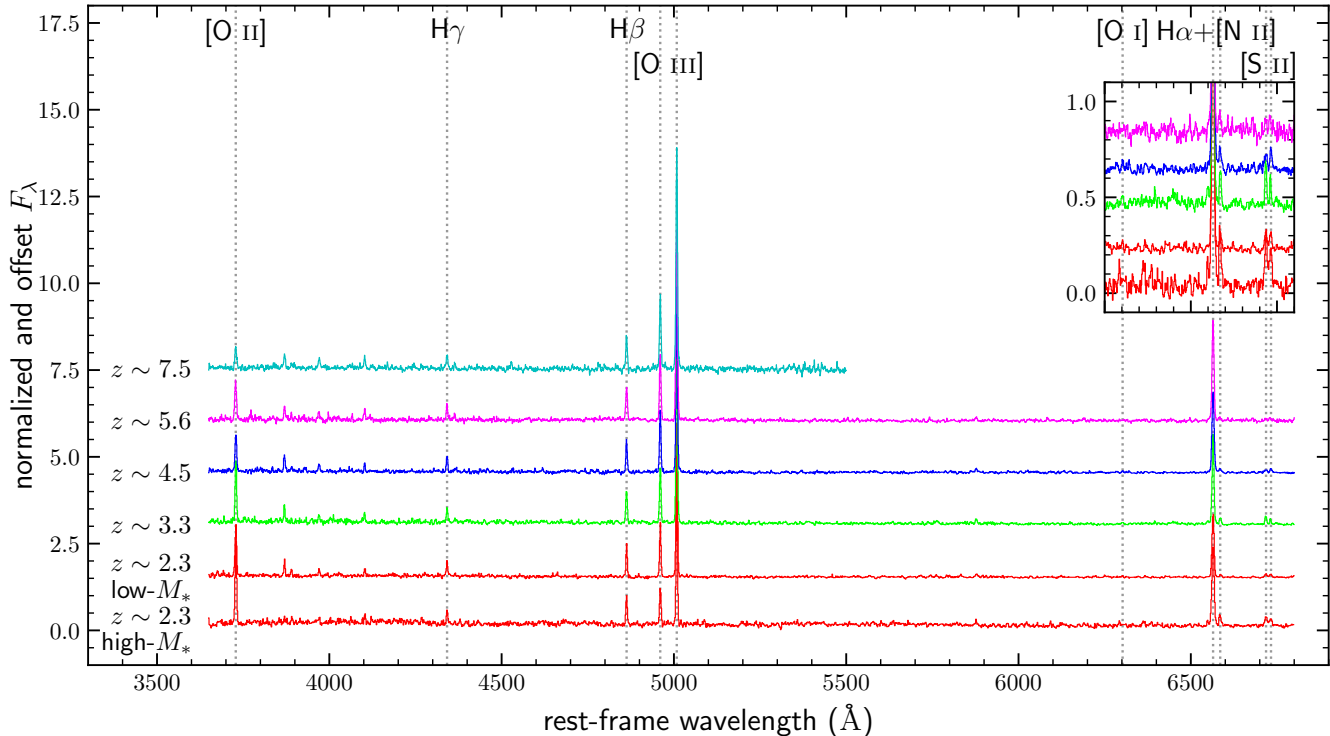


Figure 1. Composite spectra of samples in each redshift interval, constructed as described in Sec. 2.6. Each spectrum has been normalized to the measured $H\beta$ intensity and offset vertically for display purposes. The inset panel zooms in on the the weak red rest-optical lines for the $z < 6.5$ composites on the same scale, vertically offset for clarity. The measured line ratios and uncertainties are reported in Table 1.

wavelength. We also compute a composite SED model by median-combining the individual best-fit SED models after normalizing by $H\alpha$ flux and shifting to the rest frame.

Line intensities are measured from the normalized composite spectrum using the same methods described in Sec. 2.2, using the composite SED as the continuum model to correct for Balmer absorption. The dust correction is achieved using the $H\alpha/H\beta$ ratio measured from the composite, and uncorrected and dust-corrected line ratios are calculated. Dust-corrected $SFR(H\alpha)$ is calculated by multiplying the dust-corrected, normalized $H\alpha$ intensity by the median $H\alpha$ flux of the individual objects, converting to luminosity using the median redshift of the individual targets, and assuming the low-metallicity conversion factor described in Sec. 2.4. Uncertainties on all properties derived from composite spectra are estimated by bootstrap resampling the targets with replacement, perturbing the individual spectra according to the error spectra, repeating the stacking process and remeasuring all line intensities and derived quantities. This process was repeated 500 times, and the uncertainty on each quantity was taken to be the interior 68th-percentile bounds on the resulting distributions. The composite uncertainties thus represent the

combination of both measurement uncertainty and sample variance. Because of differences in rest-frame wavelength coverage due to redshift and position on the slit-mask, chip gaps, and masked regions in the 1D spectra, every galaxy in a bin does not contribute to the composite at every wavelength. However, over the wavelength range used in this analysis, $> 85\%$ of the galaxies included in each composite contribute at each wavelength such that the resulting composite represents an unbiased sample-average of the individual sources. The detector chip gap covers $\approx 10\%$ of the total accessible wavelength range in each medium-resolution grating configuration, such that the deficit in total galaxies at any particular wavelength in this range is predominantly due to the lack of spectral information in the chip gap.

The $z \sim 2.3$ spectra are of sufficient depth to detect $[N II]$ and $[S II]$ after dividing the sample into two bins. We choose to divide the $z \sim 2.3$ sample into two bins at the median stellar mass, and consequently require $S/N \geq 3$ for $H\alpha$ and a measured stellar mass from SED fitting, resulting in a $z \sim 2.3$ stacking sample of 26 out of the 29 targets at this redshift. For the higher redshift intervals, $[N II]$ and $[S II]$ were not detected in all composites when dividing into two stellar mass bins. Accordingly, we stack all $z \geq 2.7$ galaxies in a single bin per

Table 1. Properties of composite spectra for the CEERS/NIRSpec targets at $z = 2.0 - 9.3$.

sample	N_{gal}^a	z_{med}	$\log\left(\frac{M_*}{M_{\odot}}\right)^b$	$\log\left(\frac{\text{SFR}(\text{H}\alpha)}{M_{\odot}/\text{yr}}\right)$	$\log\left(\frac{[\text{O III}]}{\text{H}\beta}\right)$	$\log\left(\frac{[\text{N II}]}{\text{H}\alpha}\right)$	$\log\left(\frac{[\text{S II}]}{\text{H}\alpha}\right)$	$\log\left(\frac{[\text{O I}]}{\text{H}\alpha}\right)$	$\log(\text{R}_{32})$	$\log(\text{O}_{32})$
$z \sim 2.3$ (high- M_*)	13	2.337	$9.78^{+0.05}_{-0.01}$	$0.73^{+0.03}_{-0.08}$	$0.58^{+0.02}_{-0.03}$	$-0.93^{+0.04}_{-0.11}$	$-0.68^{+0.04}_{-0.03}$	< -1.52	$0.94^{+0.03}_{-0.04}$	$-0.03^{+0.04}_{-0.02}$
$z \sim 2.3$ (low- M_*)	13	2.302	$9.09^{+0.04}_{-0.07}$	$0.32^{+0.04}_{-0.04}$	$0.73^{+0.02}_{-0.02}$	$-1.39^{+0.08}_{-0.06}$	$-0.97^{+0.04}_{-0.05}$	< -1.87	$0.95^{+0.02}_{-0.02}$	$0.45^{+0.03}_{-0.03}$
$z \sim 3.3$	27	3.321	$9.64^{+0.04}_{-0.08}$	$0.61^{+0.06}_{-0.04}$	$0.68^{+0.02}_{-0.01}$	$-1.18^{+0.03}_{-0.06}$	$-0.92^{+0.04}_{-0.05}$	$-1.75^{+0.15}_{-0.12}$	$0.91^{+0.03}_{-0.01}$	$0.40^{+0.02}_{-0.04}$
$z \sim 4.5$	31	4.560	$9.41^{+0.12}_{-0.06}$	$0.75^{+0.07}_{-0.04}$	$0.78^{+0.03}_{-0.01}$	$-1.29^{+0.05}_{-0.07}$	$-1.08^{+0.05}_{-0.05}$	< -1.80	$0.98^{+0.04}_{-0.01}$	$0.49^{+0.03}_{-0.04}$
$z \sim 5.6$	38	5.507	$8.57^{+0.04}_{-0.13}$	$0.67^{+0.04}_{-0.05}$	$0.75^{+0.02}_{-0.02}$	$-1.46^{+0.12}_{-0.09}$	$-1.30^{+0.17}_{-0.02}$	< -1.67	$0.95^{+0.01}_{-0.02}$	$0.52^{+0.07}_{-0.01}$
$z \sim 7.5$	24	7.461	—	—	$0.81^{+0.03}_{-0.02}$	—	—	—	$0.97^{+0.03}_{-0.02}$	$0.94^{+0.10}_{-0.09}$

^a Number of galaxies in each composite. ^b Median stellar mass of galaxies in each composite.

redshift interval to achieve sufficient S/N for the weak lines, requiring only that H α has $\text{S/N} \geq 3$ for normalization. This selection results in stacking samples of 27 out of 29 galaxies at $z \sim 3.3$, 31 out of 36 galaxies at $z \sim 4.5$, and 38 out of 43 galaxies at $z \sim 5.6$. Since H α is not covered at $z > 6.5$, we instead use [O III] λ 5008 normalization throughout the stacking process, the composite H γ /H β ratio for dust correction, and $\text{SFR}(\text{H}\beta)$ in this highest redshift bin. The requirement of [O III] λ 5008 $\text{S/N} \geq 3$ yields a stacking sample of 24 out of 27 galaxies at $z \sim 7.5$.

The composite spectra in each of these bins are displayed in Figure 1, showing significant detections of [O II], H β , and [O III] λ 4960,5008 in all bins, as well as H α , [N II] λ 6585, and [S II] λ 6718,6733 in the $z < 6.5$ bins. Ratios of these lines are the subject of this analysis, and are reported in Table 1 alongside stellar mass, SFR, and redshift. Many weaker lines including [Ne III] λ 3870, higher-order Balmer lines, [O III] λ 4363, and He I λ 5877 are also present and will be the subject of future studies.

2.7. Low-redshift Comparison Samples

We compared to $z \sim 0$ star-forming galaxies selected from the Sloan Digital Sky Survey (SDSS York et al. 2000) using the selection criterion of Andrews & Martini (2013), resulting in a sample of $\approx 200,000$ star-forming galaxies at $z \sim 0.07$. We use emission-line measurements and stellar masses from the MPA-JHU catalogs⁴ and calculate reddening-corrected line ratios and $\text{SFR}(\text{H}\alpha)$ as described above, adopting the solar-metallicity $\text{SFR}(\text{H}\alpha)$ conversion factor (Sec. 2.4). We also compare to the collection of ~ 1000 $z = 0$ H II re-

gions presented in Sanders et al. (2017), an expansion of the catalog of Pilyugin & Grebel (2016). Line ratios are calculated from the dust-corrected line intensities tabulated in this catalog.

3. RESULTS

3.1. Sample Properties

We begin by investigating the sample properties of the galaxies in each redshift interval. Before analyzing the excitation properties of the sample, it is of interest to understand whether these galaxies lie along the “main sequence” of star formation in the SFR vs. M_* plane because gas-phase metallicity and ionization state have been found to depend on SFR and/or specific SFR ($\text{sSFR} = \text{SFR}/M_*$) (e.g., Mannucci et al. 2010; Sanders et al. 2016, 2021; Kashino & Inoue 2019). Figure 2 shows SFR vs. M_* for the individual galaxies and composites at $z = 2.0 - 6.5$. For individual galaxies, both $\text{SFR}(\text{H}\alpha)$ (filled circles) and $\text{SFR}(\text{SED})$ (hollow squares) are shown. SFR and M_* display positive correlations at each redshift, with H α - and SED-derived SFRs showing good agreement on average. We compare these measurements to the parameterized star-forming main sequence of Speagle et al. (2014) evaluated at the median redshift of each bin. For the lowest two redshift intervals, we also compare to Balmer-line SFR measurements from stacked spectra of star-forming galaxies from the MOSDEF survey at $z \sim 2.3$ and $z \sim 3.3$ from Sanders et al. (2021). Both the Speagle et al. (2014) relation and the MOSDEF stacks have been adjusted 0.34 dex lower in SFR to account for the difference between the solar-metallicity Hao et al. (2011) SFR conversion factor on which those works are based and the low-metallicity BPASS conversion factor that is predominantly used here.

⁴ <https://wwwmpa.mpa-garching.mpg.de/SDSS/DR7/>

The CEERS/NIRSpec samples at $z \sim 2.3$, $z \sim 3.3$, and $z \sim 4.5$ are representative of main sequence galaxies at these redshifts, with individual targets scattering about the mean relation while the composites show good agreement with the [Speagle et al. \(2014\)](#) relation. The $z \sim 2.3$ and $z \sim 3.3$ CEERS targets further display excellent agreement with the main-sequence MOSDEF samples matched in redshift. At $z \sim 5.6$, the CEERS sample lies mostly above the main sequence, with the composite having 0.4 dex higher SFR at fixed M_* . This offset is likely the result of the lower average M_* of the $z \sim 5.6$ sample combined with the higher limiting line luminosity at this higher redshift, relative to the $z < 5.0$ samples. We thus find that the CEERS/NIRSpec targets at $z = 2.0 - 5.0$ are representative of the main-sequence star-forming galaxy population, while the $z \sim 5.6$ sample is moderately biased toward high sSFR. The $z \sim 7.5$ sample was excluded from this analysis due to the lack of a robust determination of the main sequence at such high redshifts (the [Speagle et al. \(2014\)](#) analysis only included data up to $z \sim 6$). However, it is likely that the $z \sim 7.5$ is also biased toward starbursts like the $z \sim 5.6$ sample.

3.2. The BPT Diagrams at $z = 2.0 - 6.5$

We now turn to the excitation properties of the CEERS/NIRSpec galaxies as revealed by their emission-line ratios. Figure 3 displays the $z = 2.0 - 6.5$ samples and composite spectra in the [N II], [S II], and [O I] BPT diagrams separately for each redshift interval, alongside the $z \sim 0$ SDSS star-forming galaxies. At $z \sim 2.3$, the CEERS targets display decreasing [O III]/H β with increasing [N II]/H α along a sequence that is offset from the $z \sim 0$ locus toward higher [N II]/H α at fixed [O III]/H β (or, equivalently, higher [O III]/H β at fixed [N II]/H α). [O III]/H β also decreases with increasing [S II]/H α , with the $z \sim 2.3$ galaxies lying along the $z \sim 0$ locus. These trends are in agreement with past studies at $z \sim 2.3$ using ground-based spectroscopy of hundreds of galaxies (e.g., [Shapley et al. 2015, 2019](#); [Steidel et al. 2014](#); [Strom et al. 2017, 2018](#); [Sanders et al. 2016](#)). While [O I] λ 6302 is not significantly detected in either $z \sim 2.3$ composite, 3σ upper limits suggest that $z \sim 2.3$ galaxies lie below the [Kewley et al. \(2006\)](#) demarcation between local star-forming galaxies and AGN in the [O I] BPT diagram.

Before the advent of *JWST*, it was not possible to measure the lines required for BPT diagrams at $z > 2.7$. We now present the first statistical results on the position of star-forming galaxies in these diagnostic excitation diagrams at $z = 2.7 - 6.5$. Galaxies at $z \sim 3.3$ also display a clear trend of decreasing [O III]/H β with

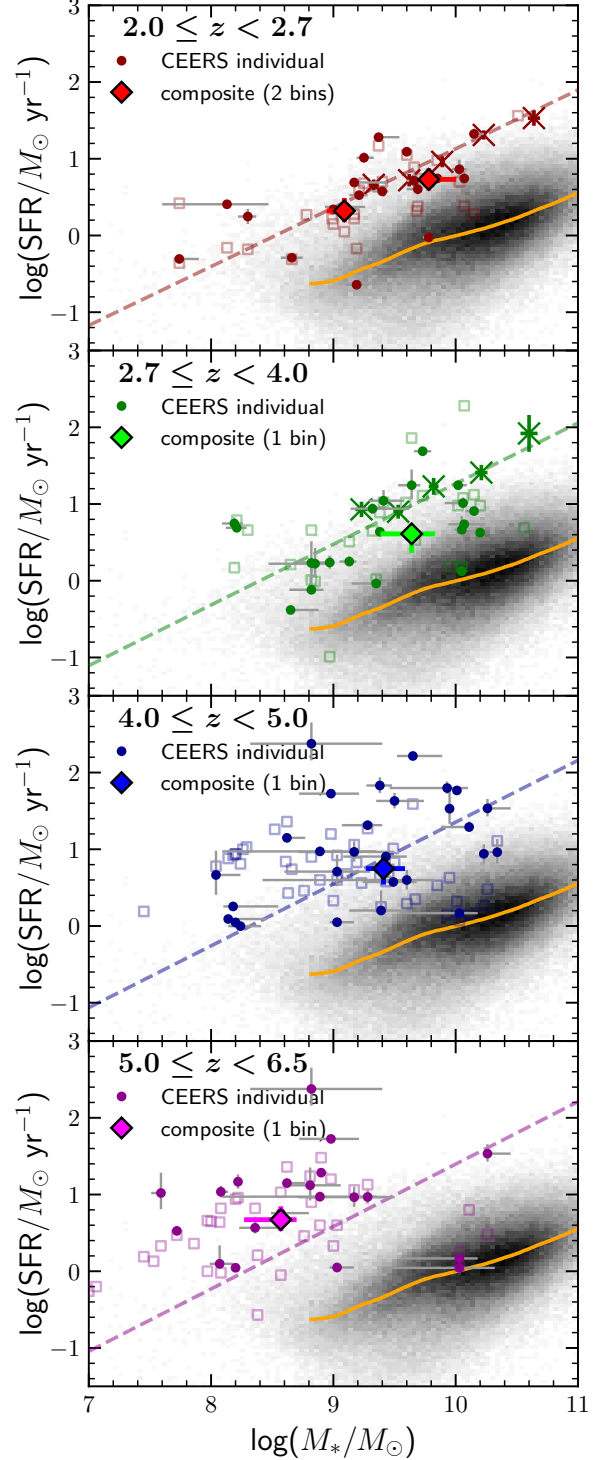


Figure 2. SFR vs. M_* for samples at $z = 2.0 - 6.5$. Filled circles with error bars display SFR(H α), while hollow squares present SFR(SED). In each panel, the dashed line displays the star-forming main sequence from the parameterization of [Speagle et al. \(2014\)](#), calculated at the median redshift of the galaxies in each bin. The gray two-dimensional histogram displays the distribution of $z \sim 0$ star-forming galaxies from SDSS, for which the orange line shows the median trend.

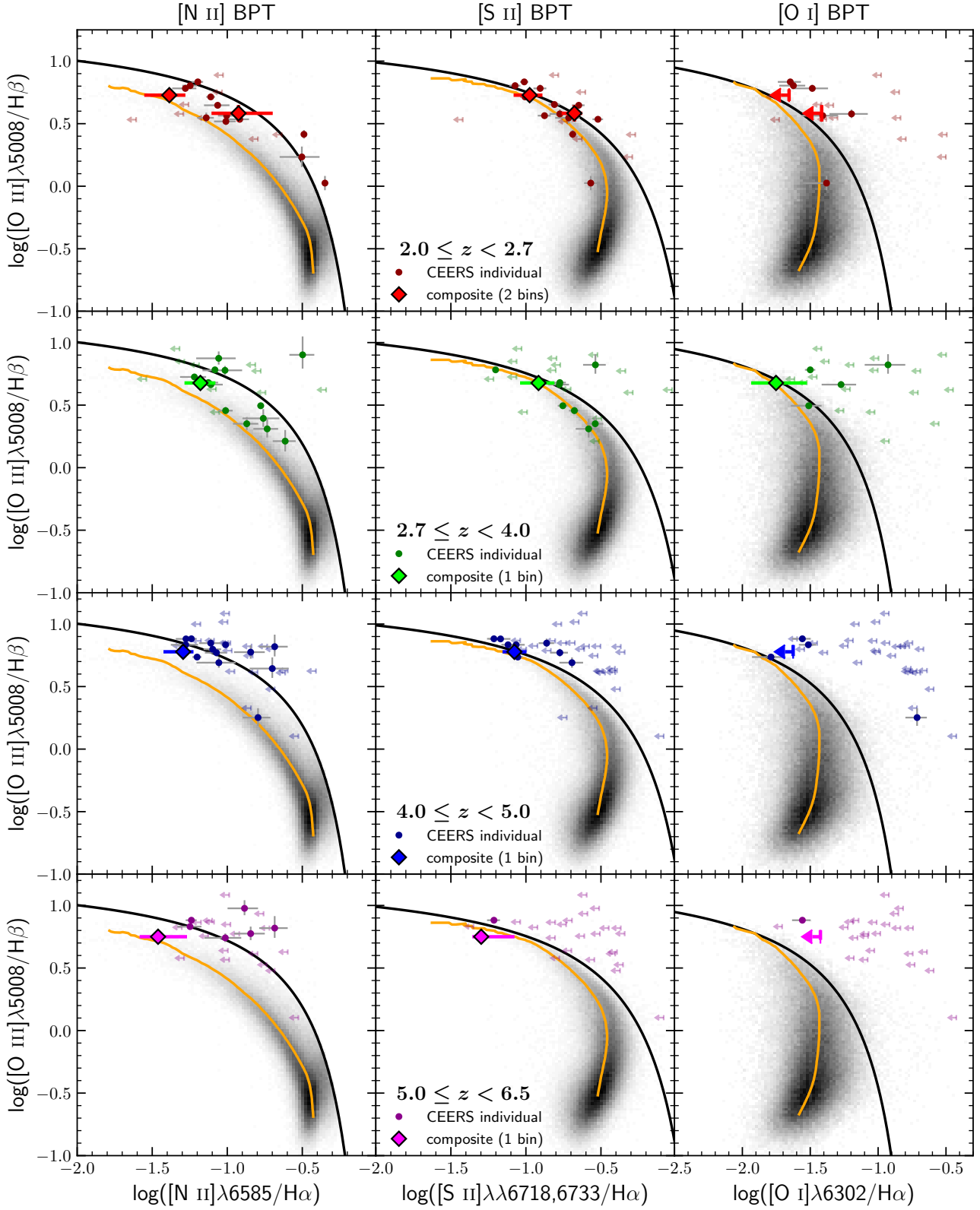


Figure 3. The [N II] (left column), [S II] (middle column), and [O I] (right column) BPT diagrams at $z = 2.0 - 6.5$. Each row displays individual galaxies and composite spectra for a single redshift interval. Arrows denote 3σ upper limits when the weakest line was not detected. The gray two-dimensional histogram shows the distribution of $z \sim 0$ star-forming galaxies from SDSS, while the orange line provides the median trend of this sample. The black solid line displays the local empirical demarcation between star-forming galaxies and AGN from [Kauffmann et al. \(2003\)](#) ([N II] BPT) or [Kewley et al. \(2006\)](#) ([S II] and [O I] BPT diagrams).

increasing $[\text{N II}]/\text{H}\alpha$ and $[\text{S II}]/\text{H}\alpha$. At $z \sim 4.5$ and $z \sim 5.6$, such trends cannot be reliably assessed with the current sample due to the large number of upper limits on $[\text{N II}]$ and/or $[\text{S II}]$ and the inability to detect these lines in stacks of more than a single bin, motivating the collection of a considerably larger statistical sample to understand the shape of the BPT excitation sequences at these redshifts. However, the single-bin stacks allow us to assess average offsets relative to the local BPT sequences. Galaxies at $z \sim 3.3$, $z \sim 4.5$, and $z \sim 5.6$ are all offset above the $[\text{N II}]$ BPT sequence on average, similar to what has been found at $z \sim 2.3$, while the composites are consistent with no offset relative to $z \sim 0$ in the $[\text{S II}]$ BPT diagram at each of these redshifts. The $z \sim 3.3$ composite further displays no offset in the $[\text{O I}]$ BPT diagram. In all $z > 2$ samples, individual galaxies with no evidence of significant AGN emission scatter above the local demarcations between AGN and star-forming galaxies derived by [Kauffmann et al. \(2003\)](#) and [Kewley et al. \(2006\)](#). While reliable alternative AGN identification information (e.g., X-ray, rest-near-IR colors) are not as readily available at $z > 4$, this result suggests that the $z \sim 0$ BPT diagram demarcations are not reliable separators of star-forming galaxies and AGN in the high-redshift universe, consistent with earlier findings at $z \sim 2.3$ ([Coil et al. 2015](#)).

Figure 4 compares individual detections and composites of the CEERS $z = 2.0 - 6.5$ samples to $z \sim 0$ star-forming galaxies and H II regions, as well as ground-based composites from the MOSDEF survey in the $[\text{N II}]$ and $[\text{S II}]$ BPT diagrams ([Shapley et al. 2015](#)). As shown by [Shapley et al. \(2015\)](#), the MOSDEF samples reveal a steady evolution of the BPT excitation sequence toward higher $[\text{O III}]/\text{H}\beta$ and $[\text{N II}]/\text{H}\alpha$ from $z \sim 0$ to $z \sim 1.5$ to $z \sim 2.3$. The $z \sim 2.3$ CEERS stacks are consistent with the $z \sim 2.3$ MOSDEF sequence, though the CEERS data extend to lower $[\text{N II}]/\text{H}\alpha$ as a consequence of its lower M_* range, which includes lower-metallicity galaxies than those in MOSDEF. The $z > 4.0$ samples in particular lie predominantly at lower M_* and $[\text{N II}]/\text{H}\alpha$ than MOSDEF. We consider the combined $z \sim 2.3$ CEERS+MOSDEF composites as defining a single excitation sequence at this redshift in which the low- M_* CEERS composite extends the MOSDEF sequence to lower $[\text{N II}]/\text{H}\alpha$. The $z \sim 3.3$, $z \sim 4.5$, and $z \sim 5.6$ composites are all consistent with this combined $z \sim 2.3$ sequence within the uncertainties, suggesting no strong evolution of the $[\text{N II}]$ BPT excitation sequence at redshifts higher than $z \sim 2.3$ within the precision limits of the current samples.

In the $[\text{S II}]$ BPT diagram, we again find that the CEERS samples at $z = 2.0 - 6.5$ appear to lie on the

same excitation sequence. This high-redshift $[\text{S II}]$ sequence is consistent with the locus of low-metallicity $z \sim 0$ galaxies from SDSS but significantly offset toward higher $[\text{S II}]/\text{H}\alpha$ at fixed $[\text{O III}]/\text{H}\beta$ relative to $z = 0$ H II regions, similar to findings at $z \sim 2$ by [Shapley et al. \(2019\)](#). In the $[\text{O I}]$ BPT diagram, the composite detection at $z \sim 3.3$ yields a similar result, being consistent with the $z \sim 0$ star-forming galaxies but offset from the local H II regions.

3.3. The $O_{32}-R_{23}$ Diagram

The position of CEERS galaxies and composites at $z = 2.0 - 9.3$ in the O_{32} vs. R_{23} diagram is shown separately for each redshift interval in Figure 5, now including the $z \sim 7.5$ sample for which the necessary lines in this diagram are still accessible with NIRSspec. At each redshift, the CEERS galaxies lie near the excitation sequence described by the median relation of the $z \sim 0$ SDSS star-forming galaxies, though a non-negligible fraction of high-redshift sources have very high $R_{23} > 10$ where local star-forming sources are exceedingly rare. Figure 6 displays all five high-redshift samples alongside local samples and stacked measurements from the MOSDEF survey at $z \sim 2.3$ and $z \sim 3.3$ ([Sanders et al. 2021](#)). We find that $z = 2 - 4$ targets are offset from the $z \sim 0$ SDSS sequence toward higher R_{23} at fixed O_{32} at $\log(O_{32}) \lesssim 0.2$, but this offset appears to decrease toward higher O_{32} until the high-redshift samples are coincident with the median $z \sim 0$ SDSS sequence. However, both the SDSS and high-redshift galaxies are offset from the $z = 0$ H II regions toward higher R_{23} at fixed O_{32} . As in the BPT diagrams, no significant evolution is apparent above $z = 2.0$, with the composites at $z \sim 2.3$ (low- M_*), $z \sim 3.3$, $z \sim 4.5$, and $z \sim 5.6$ in particular falling in a nearly identical position. Interestingly, the $z \sim 7.5$ sample lies at significantly higher O_{32} than the $z < 6.5$ samples, with an average $O_{32} \approx 10$.

4. DISCUSSION

The rest-frame optical emission-line ratio measurements from *JWST*/NIRSspec presented above enable the first glimpse of the metallicity, excitation, and ionization properties of the typical star-forming galaxy population at $z > 4$ based on rest-optical emission lines, and an expanded view at $z = 2.7 - 4$ where rest-optical lines redward of $[\text{O III}]\lambda 5008$ were inaccessible prior to *JWST*. The $z > 2.7$ samples uniformly display weak $[\text{N II}]$ ($\log([\text{N II}]/\text{H}\alpha) < -1.0$) and $[\text{S II}]$ ($\log([\text{S II}]/\text{H}\alpha) < -0.8$), and high $[\text{O III}]/\text{H}\beta$ ($\gtrsim 3$), R_{23} ($\gtrsim 6$), and O_{32} ($\gtrsim 2$). This pattern of emission-line strengths indicates that low gas-phase metallicities and high degrees of ionization are common among early-

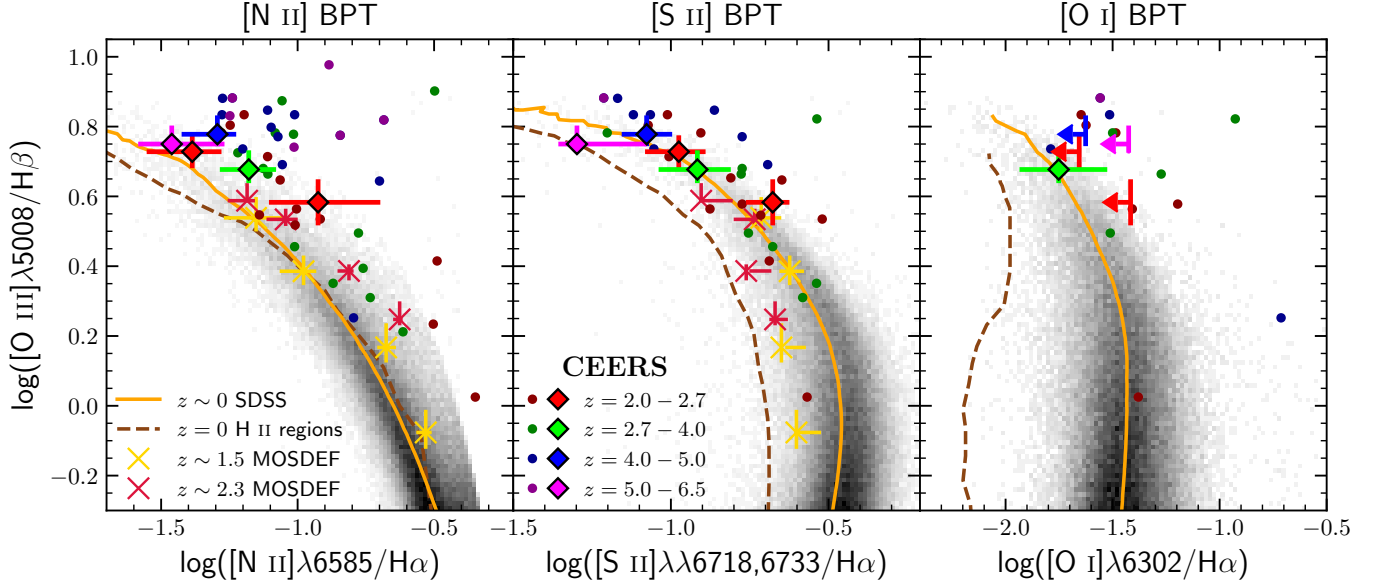


Figure 4. The [N II] (left), [S II] (middle), and [O I] (right) BPT diagrams for samples at $z = 0 - 6.5$. Composite spectra and individually-detected CEERS galaxies are displayed as in Fig. 3. Composite spectra of star-forming galaxies at $z \sim 1.5$ and $z \sim 2.3$ from the MOSDEF survey are displayed as "X"s (Shapley et al. 2019). The distribution of $z \sim 0$ star-forming galaxies from SDSS is shown in the gray two-dimensional histogram, with the median trend provided in orange. The brown dashed line denotes the median line ratio sequences derived from the catalog of ~ 1000 $z = 0$ H II regions presented in Sanders et al. (2017) (see also Pilyugin & Grebel 2016).

universe galaxies, qualitatively consistent with expectations based on the evolution of the mass-metallicity relation (Sanders et al. 2021) and the anti-correlation between metallicity and ionization parameter (Pérez-Montero 2014). However, the fact that $[\text{O III}]/\text{H}\beta$ and R_{23} remain high in all CEERS/NIRSpec samples (including at $6.5 \leq z < 9.3$) suggests that these galaxies are not extremely metal-poor in oxygen ($12 + \log(\text{O}/\text{H}) < 7.7$ or $< 0.1 Z_{\odot}$). Both $[\text{O III}]/\text{H}\beta$ and R_{23} are double valued, where these line ratios increase with increasing metallicity at $12 + \log(\text{O}/\text{H}) \lesssim 8.0$ ($0.2 Z_{\odot}$), while decreasing at higher metallicities (e.g., Kewley et al. 2019). The uniformly high values of $[\text{O III}]/\text{H}\beta$ and R_{23} across the CEERS/NIRSpec samples thus imply metallicities of $\sim 0.1 - 0.3 Z_{\odot}$ where these line ratios peak in local samples (e.g., Pilyugin & Grebel 2016). In contrast, extremely metal-poor local galaxies at $< 0.05 Z_{\odot}$ display significantly lower R_{23} and $[\text{O III}]/\text{H}\beta$ (e.g., Izotov et al. 2012, 2018), while the galaxy SMACS-0723-04590 at $z = 8.496$ with a direct-method metallicity of $12 + \log(\text{O}/\text{H}) \sim 7.0$ ($0.02 Z_{\odot}$) has $\log(R_{23}) \sim 0.6$ (Curti et al. 2023), lower than nearly all CEERS/NIRSpec galaxies at $z = 2 - 9.3$. However, the relations between these strong-line ratios and gas-phase metallicity is not yet well-constrained at $z > 2$ (Sanders et al. 2020). A significantly expanded sample of high-redshift galaxies with robust direct-method metallicity measurements is required to accurately translate the set of line ratios pre-

sented here into quantitative metallicity and ionization parameter constraints.

It is notable that, in all of the high-redshift intervals, the detection rate of all lines required to derive R_{23} and O_{32} is much higher than for [N II] and [S II]. As such, at $z > 2$, the bluer rest-optical lines ($[\text{O II}]$, $\text{H}\beta$, and $[\text{O III}]$) appear to present a significantly more viable route to metallicity and ionization information than indicators based on [N II] or [S II], while also having the advantage of being accessible at $z > 6.5$ and far into the reionization epoch. As noted above, the CEERS/NIRSpec sample at $z = 6.5 - 9.3$ displays significantly higher O_{32} on average than the sample at $z \sim 5.6$, while the $z \sim 5.6$ sample has similar O_{32} to the $z = 2.7 - 5$ galaxies. Extreme levels of ionization are thus common among the CEERS/NIRSpec $z > 6.5$ sample, but it is not clear whether this result indicates such high ionization is common among all reionization-era galaxies since we do not know whether the CEERS $z > 6.5$ sources are representative of the star-forming population. Extreme O_{32} values may indicate the presence of density-bounded H II regions that enable significant escape of Lyman-continuum (LyC) photons (Nakajima & Ouchi 2014). However, results at lower redshift suggest high O_{32} may be a necessary but not sufficient condition for significant LyC escape and similarly high O_{32} values can be produced in models with no LyC escape (e.g., Stasińska et al. 2015; Tang et al. 2019; Izotov et al. 2021; Flury

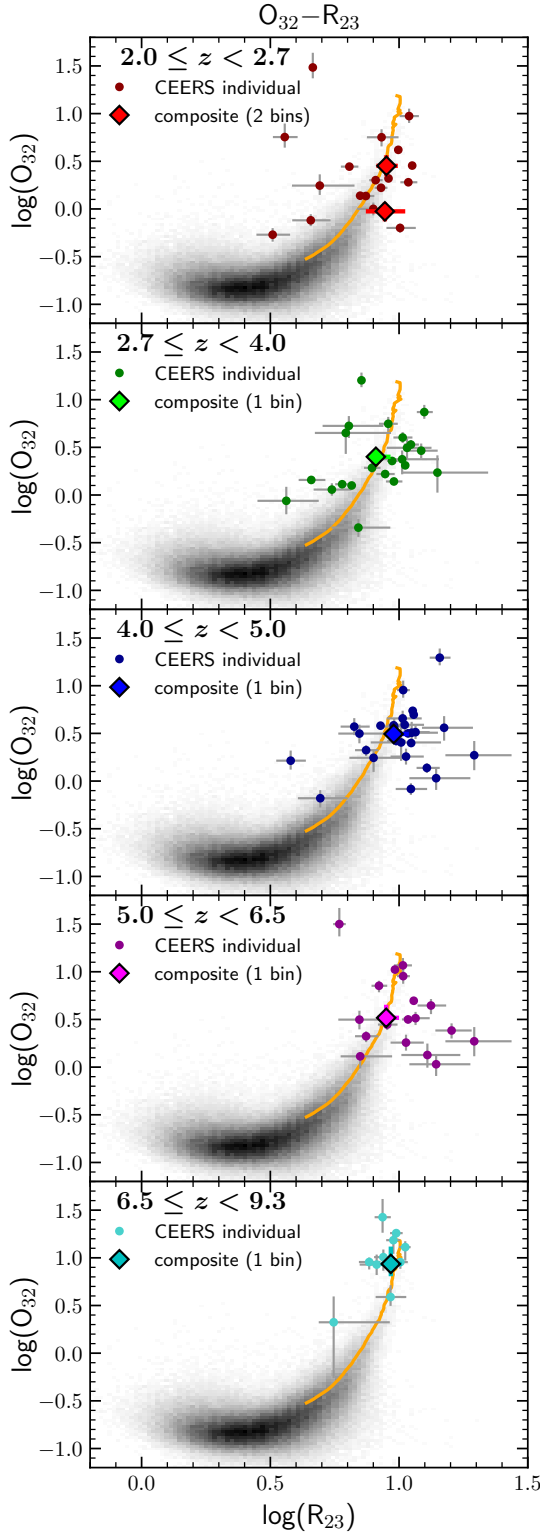


Figure 5. The O_{32} vs. R_{23} diagram at $z = 2.0 - 9.3$. Both line ratios have been corrected for dust reddening. Each row displays individual galaxies and composite spectra for a single redshift interval. The gray two-dimensional histogram and orange line shows $z \sim 0$ star-forming galaxies as in previous figures.

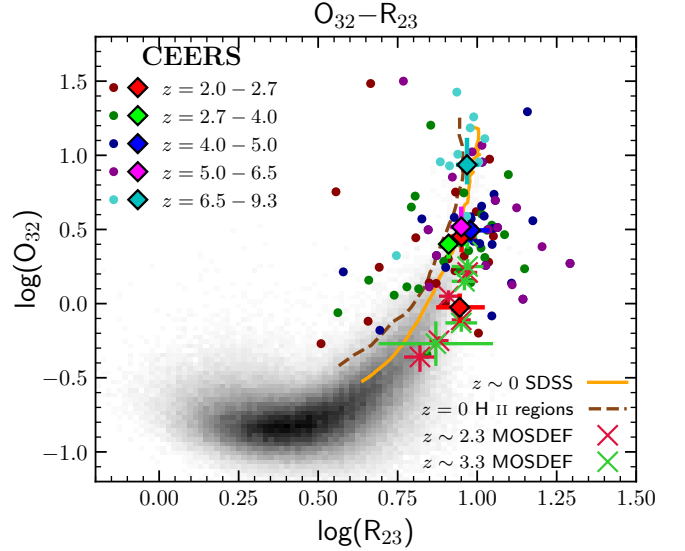


Figure 6. The O_{32} vs. R_{23} diagram for samples at $z = 0 - 9.3$. Composite spectra and individually-detected CEERS galaxies are displayed as in Fig. 5. Composite spectra of star-forming galaxies at $z \sim 2.3$ and $z \sim 3.3$ from the MOSDEF survey are displayed as "X"s (Sanders et al. 2021). The distribution of $z \sim 0$ star-forming galaxies from SDSS is shown in the gray two-dimensional histogram, with the median trend provided in orange. The brown dashed line denotes the median sequence $z = 0$ H II regions.

et al. 2022). The seemingly rapid increase in the degree of ionization between $z \sim 5.6$ and $z > 6.5$ among the CEERS galaxies thus does not necessarily indicate an increase in LyC escape.

A key result is that all CEERS/NIRSpec samples spanning $z = 2.0 - 6.5$ fall along the same sequence in the [N II] and [S II] BPT diagrams, as well as in the O_{32} - R_{23} diagram. Specifically, the $z \sim 3.3$, $z \sim 4.5$, and $z \sim 5.6$ composites all have line ratios that are consistent within the uncertainties with the low- M_* $z \sim 2.3$ composite in all line ratio diagrams presented here. The similar line ratio properties of these samples suggest that the ionization conditions of gas in H II regions do not significantly evolve between $z = 2$ and $z = 6.5$, spanning 2.4 Gyr of cosmic history. If this result is confirmed with expanded future samples, then one important implication is that the same diagnostic calibrations can be used to translate strong-line ratios into physical properties such as metallicity and ionization parameter across this wide redshift range.

We find that the unified $z > 2$ excitation sequence is offset toward higher [N II]/ $H\alpha$ at fixed [O III]/ $H\beta$ relative to $z \sim 0$ SDSS star-forming galaxies, but lies on the $z \sim 0$ locus in the [S II] BPT diagram (and the [O I] BPT diagram for the $z \sim 3.3$ composite). This comparison is complicated by the presence of diffuse ionized

gas (DIG) emission in the galaxy-integrated SDSS fiber spectra, significantly affecting galaxy-integrated line ratios (Zhang et al. 2017; Sanders et al. 2017; Vale Asari et al. 2019; Belfiore et al. 2022). Shapley et al. (2019) argued that the high-SFR nature of high-redshift galaxies suggests negligible DIG emission in their integrated spectra, such that a comparison should instead be made to local H II regions or SDSS spectra that have been corrected for DIG contamination. It can be seen in Figures 4 and 6 that the CEERS/NIRSpec samples are in fact offset from the median sequence of $z = 0$ H II regions in each of these line ratio diagrams, with higher [N II]/H α , [S II]/H α , and [O I]/H α at fixed [O III]/H β and larger R₂₃ at fixed O₃₂.

These offsets with respect to $z = 0$ H II regions are consistent with high-redshift galaxies uniformly having a harder ionizing spectrum at fixed O/H, driving larger [O III]/H β , [N II]/H α , [S II]/H α , and R₂₃ (e.g., Steidel et al. 2016). At $z \sim 2 - 3.5$, recent studies have shown that massive stars in these galaxies have chemical compositions with elevated α /Fe ratios of $O/Fe \approx 2 - 5 \times O/Fe_{\odot}$ (Steidel et al. 2016; Strom et al. 2018, 2022; Topping et al. 2020a,b; Sanders et al. 2020; Cullen et al. 2021; Reddy et al. 2022). This α -enhancement and Fe-deficiency is a consequence of the short formation timescales of high-redshift galaxies, in which enrichment is dominated by short-timescale core-collapse supernovae while time-delayed Type Ia supernovae have not yet significantly enriched the ISM in Fe.

Our results are thus consistent with α -enhanced massive stars driving offsets between local and $z = 2.0 - 6.5$ samples in the BPT and O₃₂-R₂₃ diagrams, as expected if galaxies are typically younger at higher redshifts. However, such a trend may be expected to lead to higher levels of α -enhancement at higher redshifts, and thus a steadily increasing excitation sequence offset above $z = 2$ for which we do not find evidence. It may be that the theoretical upper-limit on α -enhancement from

pure core-collapse supernovae enrichment ($\approx 5 \times O/Fe_{\odot}$; Kobayashi et al. 2020) is reached at typical galaxy ages at $\sim 2 - 4$ such that younger stellar populations at $z \sim 4 - 6.5$ do not lead to higher α/Fe , or that the precision enabled by the current $z > 2.7$ sample sizes (~ 30 galaxies per redshift interval) is not great enough to resolve the shift in line ratios based on evolution from $\approx 3 \times O/Fe_{\odot}$ at $z \sim 2$ to $5 \times O/Fe_{\odot}$ at some higher redshift. The present sample is also too small to detect weak lines ([N II], [S II], [O I]) in multiple bins at $z > 2.7$ to test whether the shape of these excitation sequences remains the same over $z = 2 - 6.5$. An order-of-magnitude larger sample is ultimately needed to approach the level of statistical power reached by ground-based samples at $z \sim 2.3$ (e.g., Steidel et al. 2014; Shapley et al. 2019) and establish the shape and relative offset of $z > 2.7$ excitation sequences with high precision. *JWST*/NIRSpec has the capability to provide such a sample and transform our understanding of the chemical and ionization properties of early galaxies in the coming years.

This work is based on observations made with the NASA/ESA/CSA James Webb Space Telescope. The data were obtained from the Mikulski Archive for Space Telescopes at the Space Telescope Science Institute, which is operated by the Association of Universities for Research in Astronomy, Inc., under NASA contract NAS5-03127 for *JWST*. Support for this work was provided through the NASA Hubble Fellowship grant #HST-HF2-51469.001-A awarded by the Space Telescope Science Institute, which is operated by the Association of Universities for Research in Astronomy, Incorporated, under NASA contract NAS5-26555. We also acknowledge support from NASA grant *JWST*-GO-01914.

Facilities: *JWST*(NIRSpec)

REFERENCES

- Andrews, B. H., & Martini, P. 2013, *ApJ*, 765, 140, doi: [10.1088/0004-637X/765/2/140](https://doi.org/10.1088/0004-637X/765/2/140)
- Arellano-Córdova, K. Z., Berg, D. A., Chisholm, J., et al. 2022, *ApJL*, 940, L23, doi: [10.3847/2041-8213/ac9ab2](https://doi.org/10.3847/2041-8213/ac9ab2)
- Asplund, M., Amarsi, A. M., & Grevesse, N. 2021, *A&A*, 653, A141, doi: [10.1051/0004-6361/202140445](https://doi.org/10.1051/0004-6361/202140445)
- Baldwin, J. A., Phillips, M. M., & Terlevich, R. 1981, *PASP*, 93, 5, doi: [10.1086/130766](https://doi.org/10.1086/130766)
- Belfiore, F., Santoro, F., Groves, B., et al. 2022, *A&A*, 659, A26, doi: [10.1051/0004-6361/202141859](https://doi.org/10.1051/0004-6361/202141859)
- Brinchmann, J. 2022, arXiv e-prints, arXiv:2208.07467, <https://arxiv.org/abs/2208.07467>
- Calzetti, D., Armus, L., Bohlin, R. C., et al. 2000, *ApJ*, 533, 682, doi: [10.1086/308692](https://doi.org/10.1086/308692)
- Cardelli, J. A., Clayton, G. C., & Mathis, J. S. 1989, *ApJ*, 345, 245, doi: [10.1086/167900](https://doi.org/10.1086/167900)
- Chabrier, G. 2003, *PASP*, 115, 763, doi: [10.1086/376392](https://doi.org/10.1086/376392)
- Coil, A. L., Aird, J., Reddy, N., et al. 2015, *ApJ*, 801, 35, doi: [10.1088/0004-637X/801/1/35](https://doi.org/10.1088/0004-637X/801/1/35)

- Conroy, C., Gunn, J. E., & White, M. 2009, *ApJ*, 699, 486, doi: [10.1088/0004-637X/699/1/486](https://doi.org/10.1088/0004-637X/699/1/486)
- Cullen, F., Shapley, A. E., McLure, R. J., et al. 2021, *MNRAS*, 505, 903, doi: [10.1093/mnras/stab1340](https://doi.org/10.1093/mnras/stab1340)
- Curti, M., Mannucci, F., Cresci, G., & Maiolino, R. 2020, *MNRAS*, 491, 944, doi: [10.1093/mnras/stz2910](https://doi.org/10.1093/mnras/stz2910)
- Curti, M., D'Eugenio, F., Carniani, S., et al. 2023, *MNRAS*, 518, 425, doi: [10.1093/mnras/stac2737](https://doi.org/10.1093/mnras/stac2737)
- Du, X., Shapley, A. E., Reddy, N. A., et al. 2018, *ApJ*, 860, 75, doi: [10.3847/1538-4357/aabfcf](https://doi.org/10.3847/1538-4357/aabfcf)
- Finkelstein, S. L., Bagley, M. B., Ferguson, H. C., et al. 2022a, arXiv e-prints, arXiv:2211.05792. <https://arxiv.org/abs/2211.05792>
- Finkelstein, S. L., Bagley, M. B., Haro, P. A., et al. 2022b, *ApJL*, 940, L55, doi: [10.3847/2041-8213/ac966e](https://doi.org/10.3847/2041-8213/ac966e)
- Flury, S. R., Jaskot, A. E., Ferguson, H. C., et al. 2022, *ApJ*, 930, 126, doi: [10.3847/1538-4357/ac61e4](https://doi.org/10.3847/1538-4357/ac61e4)
- Gordon, K. D., Clayton, G. C., Misselt, K. A., Landolt, A. U., & Wolff, M. J. 2003, *ApJ*, 594, 279, doi: [10.1086/376774](https://doi.org/10.1086/376774)
- Hao, C.-N., Kennicutt, R. C., Johnson, B. D., et al. 2011, *ApJ*, 741, 124, doi: [10.1088/0004-637X/741/2/124](https://doi.org/10.1088/0004-637X/741/2/124)
- Horne, K. 1986, *PASP*, 98, 609, doi: [10.1086/131801](https://doi.org/10.1086/131801)
- Izotov, Y. I., Thuan, T. X., & Guseva, N. G. 2012, *A&A*, 546, A122, doi: [10.1051/0004-6361/201219733](https://doi.org/10.1051/0004-6361/201219733)
- Izotov, Y. I., Thuan, T. X., Guseva, N. G., & Liss, S. E. 2018, *MNRAS*, 473, 1956, doi: [10.1093/mnras/stx2478](https://doi.org/10.1093/mnras/stx2478)
- Izotov, Y. I., Worseck, G., Schaerer, D., et al. 2021, *MNRAS*, 503, 1734, doi: [10.1093/mnras/stab612](https://doi.org/10.1093/mnras/stab612)
- Kashino, D., & Inoue, A. K. 2019, *MNRAS*, 486, 1053, doi: [10.1093/mnras/stz881](https://doi.org/10.1093/mnras/stz881)
- Kashino, D., Silverman, J. D., Sanders, D., et al. 2017, *ApJ*, 835, 88, doi: [10.3847/1538-4357/835/1/88](https://doi.org/10.3847/1538-4357/835/1/88)
- . 2019, *ApJS*, 241, 10, doi: [10.3847/1538-4365/ab06c4](https://doi.org/10.3847/1538-4365/ab06c4)
- Kauffmann, G., Heckman, T. M., Tremonti, C., et al. 2003, *MNRAS*, 346, 1055, doi: [10.1111/j.1365-2966.2003.07154.x](https://doi.org/10.1111/j.1365-2966.2003.07154.x)
- Kewley, L. J., Groves, B., Kauffmann, G., & Heckman, T. 2006, *MNRAS*, 372, 961, doi: [10.1111/j.1365-2966.2006.10859.x](https://doi.org/10.1111/j.1365-2966.2006.10859.x)
- Kewley, L. J., Nicholls, D. C., & Sutherland, R. S. 2019, *ARA&A*, 57, 511, doi: [10.1146/annurev-astro-081817-051832](https://doi.org/10.1146/annurev-astro-081817-051832)
- Kobayashi, C., Karakas, A. I., & Lugaro, M. 2020, *ApJ*, 900, 179, doi: [10.3847/1538-4357/abae65](https://doi.org/10.3847/1538-4357/abae65)
- Kriek, M., van Dokkum, P. G., Labbé, I., et al. 2009, *ApJ*, 700, 221, doi: [10.1088/0004-637X/700/1/221](https://doi.org/10.1088/0004-637X/700/1/221)
- Luridiana, V., Morisset, C., & Shaw, R. A. 2015, *A&A*, 573, A42, doi: [10.1051/0004-6361/201323152](https://doi.org/10.1051/0004-6361/201323152)
- Maiolino, R., Nagao, T., Grazian, A., et al. 2008, *A&A*, 488, 463, doi: [10.1051/0004-6361:200809678](https://doi.org/10.1051/0004-6361:200809678)
- Mannucci, F., Cresci, G., Maiolino, R., Marconi, A., & Gnerucci, A. 2010, *MNRAS*, 408, 2115, doi: [10.1111/j.1365-2966.2010.17291.x](https://doi.org/10.1111/j.1365-2966.2010.17291.x)
- Momcheva, I. G., Brammer, G. B., van Dokkum, P. G., et al. 2016, *ApJS*, 225, 27, doi: [10.3847/0067-0049/225/2/27](https://doi.org/10.3847/0067-0049/225/2/27)
- Nakajima, K., & Ouchi, M. 2014, *MNRAS*, 442, 900, doi: [10.1093/mnras/stu902](https://doi.org/10.1093/mnras/stu902)
- Onodera, M., Carollo, C. M., Lilly, S., et al. 2016, *ApJ*, 822, 42, doi: [10.3847/0004-637X/822/1/42](https://doi.org/10.3847/0004-637X/822/1/42)
- Pérez-Montero, E. 2014, *MNRAS*, 441, 2663, doi: [10.1093/mnras/stu753](https://doi.org/10.1093/mnras/stu753)
- Pilyugin, L. S., & Grebel, E. K. 2016, *MNRAS*, 457, 3678, doi: [10.1093/mnras/stw238](https://doi.org/10.1093/mnras/stw238)
- Reddy, N. A., Shapley, A. E., Sanders, R. L., et al. 2018, *ApJ*, 869, 92, doi: [10.3847/1538-4357/aaed1e](https://doi.org/10.3847/1538-4357/aaed1e)
- Reddy, N. A., Shapley, A. E., Kriek, M., et al. 2020, *ApJ*, 902, 123, doi: [10.3847/1538-4357/abb674](https://doi.org/10.3847/1538-4357/abb674)
- Reddy, N. A., Topping, M. W., Shapley, A. E., et al. 2022, *ApJ*, 926, 31, doi: [10.3847/1538-4357/ac3b4c](https://doi.org/10.3847/1538-4357/ac3b4c)
- Runco, J. N., Shapley, A. E., Sanders, R. L., et al. 2021, *MNRAS*, 502, 2600, doi: [10.1093/mnras/stab119](https://doi.org/10.1093/mnras/stab119)
- Sanders, R. L., Shapley, A. E., Zhang, K., & Yan, R. 2017, *ApJ*, 850, 136, doi: [10.3847/1538-4357/aa93e4](https://doi.org/10.3847/1538-4357/aa93e4)
- Sanders, R. L., Shapley, A. E., Kriek, M., et al. 2016, *ApJ*, 816, 23, doi: [10.3847/0004-637X/816/1/23](https://doi.org/10.3847/0004-637X/816/1/23)
- Sanders, R. L., Shapley, A. E., Reddy, N. A., et al. 2020, *MNRAS*, 491, 1427, doi: [10.1093/mnras/stz3032](https://doi.org/10.1093/mnras/stz3032)
- Sanders, R. L., Shapley, A. E., Jones, T., et al. 2021, *ApJ*, 914, 19, doi: [10.3847/1538-4357/abf4c1](https://doi.org/10.3847/1538-4357/abf4c1)
- Schaerer, D., Marques-Chaves, R., Barrufet, L., et al. 2022, *A&A*, 665, L4, doi: [10.1051/0004-6361/202244556](https://doi.org/10.1051/0004-6361/202244556)
- Shapley, A. E., Sanders, R. L., Reddy, N. A., Topping, M. W., & Brammer, G. B. 2023, arXiv e-prints, arXiv:2301.03241. <https://arxiv.org/abs/2301.03241>
- Shapley, A. E., Reddy, N. A., Kriek, M., et al. 2015, *ApJ*, 801, 88, doi: [10.1088/0004-637X/801/2/88](https://doi.org/10.1088/0004-637X/801/2/88)
- Shapley, A. E., Sanders, R. L., Shao, P., et al. 2019, *ApJL*, 881, L35, doi: [10.3847/2041-8213/ab385a](https://doi.org/10.3847/2041-8213/ab385a)
- Skelton, R. E., Whitaker, K. E., Momcheva, I. G., et al. 2014, *ApJS*, 214, 24, doi: [10.1088/0067-0049/214/2/24](https://doi.org/10.1088/0067-0049/214/2/24)
- Speagle, J. S., Steinhardt, C. L., Capak, P. L., & Silverman, J. D. 2014, *ApJS*, 214, 15, doi: [10.1088/0067-0049/214/2/15](https://doi.org/10.1088/0067-0049/214/2/15)
- Stasińska, G., Izotov, Y., Morisset, C., & Guseva, N. 2015, *A&A*, 576, A83, doi: [10.1051/0004-6361/201425389](https://doi.org/10.1051/0004-6361/201425389)
- Steidel, C. C., Strom, A. L., Pettini, M., et al. 2016, *ApJ*, 826, 159, doi: [10.3847/0004-637X/826/2/159](https://doi.org/10.3847/0004-637X/826/2/159)

- Steidel, C. C., Rudie, G. C., Strom, A. L., et al. 2014, *ApJ*, 795, 165, doi: [10.1088/0004-637X/795/2/165](https://doi.org/10.1088/0004-637X/795/2/165)
- Strom, A. L., Rudie, G. C., Steidel, C. C., & Trainor, R. F. 2022, *ApJ*, 925, 116, doi: [10.3847/1538-4357/ac38a3](https://doi.org/10.3847/1538-4357/ac38a3)
- Strom, A. L., Steidel, C. C., Rudie, G. C., Trainor, R. F., & Pettini, M. 2018, *ApJ*, 868, 117, doi: [10.3847/1538-4357/aae1a5](https://doi.org/10.3847/1538-4357/aae1a5)
- Strom, A. L., Steidel, C. C., Rudie, G. C., et al. 2017, *ApJ*, 836, 164, doi: [10.3847/1538-4357/836/2/164](https://doi.org/10.3847/1538-4357/836/2/164)
- Tacchella, S., Johnson, B. D., Robertson, B. E., et al. 2022, arXiv e-prints, arXiv:2208.03281. <https://arxiv.org/abs/2208.03281>
- Tang, M., Stark, D. P., Chevallard, J., & Charlot, S. 2019, *MNRAS*, 489, 2572, doi: [10.1093/mnras/stz2236](https://doi.org/10.1093/mnras/stz2236)
- Taylor, A. J., Barger, A. J., & Cowie, L. L. 2022, *ApJL*, 939, L3, doi: [10.3847/2041-8213/ac959d](https://doi.org/10.3847/2041-8213/ac959d)
- Topping, M. W., Shapley, A. E., Reddy, N. A., et al. 2020a, *MNRAS*, 495, 4430, doi: [10.1093/mnras/staa1410](https://doi.org/10.1093/mnras/staa1410)
- . 2020b, *MNRAS*, 499, 1652, doi: [10.1093/mnras/staa2941](https://doi.org/10.1093/mnras/staa2941)
- Tremonti, C. A., Heckman, T. M., Kauffmann, G., et al. 2004, *ApJ*, 613, 898, doi: [10.1086/423264](https://doi.org/10.1086/423264)
- Troncoso, P., Maiolino, R., Sommariva, V., et al. 2014, *A&A*, 563, A58, doi: [10.1051/0004-6361/201322099](https://doi.org/10.1051/0004-6361/201322099)
- Trump, J. R., Arrabal Haro, P., Simons, R. C., et al. 2022, arXiv e-prints, arXiv:2207.12388. <https://arxiv.org/abs/2207.12388>
- Vale Asari, N., Couto, G. S., Cid Fernandes, R., et al. 2019, *MNRAS*, 489, 4721, doi: [10.1093/mnras/stz2470](https://doi.org/10.1093/mnras/stz2470)
- van der Wel, A., Franx, M., van Dokkum, P. G., et al. 2014, *ApJ*, 788, 28, doi: [10.1088/0004-637X/788/1/28](https://doi.org/10.1088/0004-637X/788/1/28)
- Veilleux, S., & Osterbrock, D. E. 1987, *ApJS*, 63, 295, doi: [10.1086/191166](https://doi.org/10.1086/191166)
- Wang, X., Jones, T., Vulcani, B., et al. 2022, *ApJL*, 938, L16, doi: [10.3847/2041-8213/ac959e](https://doi.org/10.3847/2041-8213/ac959e)
- York, D. G., Adelman, J., Anderson, John E., J., et al. 2000, *AJ*, 120, 1579, doi: [10.1086/301513](https://doi.org/10.1086/301513)
- Zhang, K., Yan, R., Bundy, K., et al. 2017, *MNRAS*, 466, 3217, doi: [10.1093/mnras/stw3308](https://doi.org/10.1093/mnras/stw3308)